JOURNAL OF SYNCHROTRON RADIATION
ISSN 1600-5775

In situ coherent X-ray diffraction imaging of radiation-induced mass loss in metal–polymer composite spheres

Eirik Torbjørn Bakken Skjønsfjell,[a] Yuriy Chushkin,[b] Federico Zontone[b] and Dag Werner Breiby[a,c]*

[a]Department of Physics, Norwegian University of Science and Technology, Høgskoleringen 5, Trondheim 7491, Norway, [b]The European Synchrotron, CS 40220, 38043 Grenoble, France, and [c]Department of Microsystems, University College of South East Norway, Raveien 197, Borre 3184, Norway.
*Correspondence e-mail: dag.breiby@ntnu.no

Received 27 September 2017
Accepted 16 April 2018

Edited by G. Grübel, HASYLAB at DESY, Germany

Keywords: coherent X-ray diffraction imaging; radiation damage; X-ray photon correlation spectroscopy.

A major limitation to the use of coherent X-ray diffraction imaging (CXDI) for imaging soft materials like polymers and biological tissue is that the radiation can cause extensive damage to the sample under investigation. In this study, CXDI has been used to monitor radiation-induced structural changes in metal-coated poly(methyl methacrylate) microspheres. Using a coherent undulator X-ray beam with 8.10 keV photon energy, 14 tomograms at a resolution of ∼30 nm were measured consecutively, which resulted in an accumulated dose of 30 GGy. The three-dimensional images confirmed that the polymer core was strongly affected by the absorbed dose, giving pronounced mass loss. Specifically, as the metal–polymer composite was exposed to the X-ray beam, a bubble-like region of reduced density grew within the composite, almost filling the entire volume within the thin metallic shell in the last tomogram. The bubble seemed to have its initiation point at a hole in the metal coating, emphasizing that the free polymer surface plays an important role in the degradation process. The irradiation of an uncoated polystyrene microsphere gave further evidence for mass loss at the free surface as the radius decreased with increased dose. The CXDI study was complemented by X-ray photon correlation spectroscopy, which proved efficient in establishing exposure dose limits. Our results demonstrate that radiation-induced structural changes at the tens of nanometer scale in soft materials can be followed as a function of dose, which is important for the further development of soft-matter technology.

1. Introduction

Understanding and mitigating the effects of radiation damage are important for X-ray microscopy, in particular when dealing with soft systems like biological and organic materials that have low radiation tolerance (Jacobsen, 2016). Also, in related fields like medical imaging, reducing the radiation dose is of prime importance (Fazel *et al.*, 2009). Therefore a compromise must be found between acceptable radiation doses and the desired imaging resolution. It is clear that given a certain maximal radiation dose for a specimen there is a corresponding limit to the imaging resolution that can be obtained (Howells, Beetz *et al.*, 2009). In recent years, X-ray microscopy and tomography techniques have made significant strides towards imaging at <10 nm resolution (Miao, Ishikawa *et al.*, 2003; Takahashi, Nishino *et al.*, 2010; Takahashi, Zettsu *et al.*, 2010; Xu *et al.*, 2014; Holler *et al.*, 2014). New microscopy approaches like coherent X-ray diffractive imaging (CXDI) suffer from similar limitations when it comes to radiation

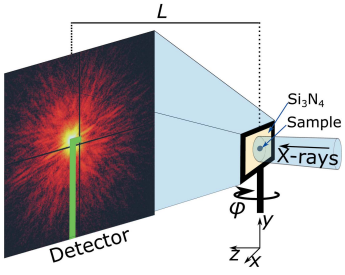

© 2018 International Union of Crystallography

damage affecting the image resolution as more established phase-contrast X-ray microscopy techniques. To circumvent the radiation damage problem, concepts like serial crystallography are currently being developed to image atomic-scale features with extremely bright beams, exploiting series of (nearly) identical samples. Although the imaged sample is likely to be destroyed when exposed to the intense X-ray beam at X-ray free-electron sources, each scattering pattern can be recorded over a period shorter than the time the sample takes to decompose (Schlichting, 2015). By repeating the imaging-before-destruction process for a large number of samples, sufficient scattering signal can be collected for analysis (Schlichting, 2015). However, serial crystallography requires a large number of identical samples, and is thus only suitable for well defined and reproducible molecules, like folded proteins. Although several studies focus on the relation between beam damage and image quality in X-ray imaging (Howells, Hitchcock *et al.*, 2009; Starodub *et al.*, 2008; Jacobsen, 2016; Shen *et al.*, 2004; Howells, Beetz *et al.*, 2009), there is still a need for systematic experimental studies that investigate the radiation effects *in situ*.

CXDI is a microscopy technique utilizing coherent X-ray scattering in the far-field regime to image the sample (Miao, Ishikawa *et al.*, 2003; Sayre & Chapman, 1995; Sayre *et al.*, 1998; Chapman *et al.*, 2006; Miao, Amonette *et al.*, 2003; Rodriguez *et al.*, 2015; Shapiro *et al.*, 2005). The recorded diffraction patterns are fed into a numerical iterative phase-retrieval algorithm, which iterates by Fourier transformations between real space and reciprocal space while applying suitable constraints to reconstruct real-space images of the electron density. Because the technique is sensitive to the phase shift of the X-ray photons propagating through the sample, it is well suited for imaging samples consisting of light elements, where the absorption contrast is too low to give a sufficient signal-to-noise ratio. CXDI has proven to be well suited for imaging biological samples (Shapiro *et al.*, 2005; Song *et al.*, 2008; Nishino *et al.*, 2009; Jiang *et al.*, 2010). Several studies have shown that CXDI is capable of sub-10 nm resolution in 2D and 3D (Miao, Ishikawa *et al.*, 2003; Takahashi, Nishino *et al.*, 2010; Takahashi, Zettsu *et al.*, 2010; Xu *et al.*, 2014). However, these high-resolution studies have been performed on radiation-tolerant inorganic test samples with large scattering cross sections, typically silver or gold. Achieving high resolution of samples consisting of lighter elements has proven more challenging (Jacobsen, 2016).

The spatial-temporal correlations of a series of scattering patterns, often applied to dilute solutions, can be studied by X-ray photon correlation spectroscopy (XPCS) (Sutton *et al.*, 1991; Leheny, 2012; Livet, 2007; Grübel & Zontone, 2004). For ergodic systems, the intensity auto-correlation function $g_2(q,\tau)$ can be analyzed through well established analytical expressions to extract, for example, diffusion constants. In the current case of structurally rigid degrading composites, the assumptions of independent scatterers and an ergodic system are clearly not fulfilled because most of the scattering material (composite core and shell) is spatially fixed during the measurement. However, the decay of $g_2(q,\tau)$ can provide information about the temporal stability under the exposure to the X-ray beam, as we shall demonstrate.

While it is true that X-rays generally interact weakly with materials, the ionizing nature of high-energy photons induces radiation damage in the irradiated material. Particularly for soft organic materials, including biological samples, radiation damage can be the limiting factor to the spatial resolution (Howells, Beetz *et al.*, 2009). Considerable efforts are thus invested into methods for reducing the absorbed dose. It is instructive to recall that radiation damage can broadly be categorized into primary and secondary effects (Jacobsen, 2016). Primary radiation damage is caused directly by absorption of X-ray photons, producing free radicals and local defects, like chain scission in the case of polymers. The absorption cross-section of X-ray photons depends only on the specific element and the radiation wavelength, and it is thus generally not possible to prevent primary radiation damage. The secondary radiation damage, on the other hand, refers to the diffusion of free radicals in the material specimen, causing additional damage, including mass loss. The secondary radiation damage can be strongly suppressed by various means, like replacing the ambient oxygen-containing atmosphere by inert gases (typically He, N_2 or Ar) to reduce the formation of oxygen radicals, or by cryogenically cooling the sample to reduce the diffusion rates (Schlichting, 2015).

Here, we present a quantitative microscopy study of metal–polymer composite microspheres, with particular attention given to the radiation-induced mass loss. The samples studied were monodisperse polymer spheres, also known as Ugelstad spheres (Ugelstad *et al.*, 1980). These beads can be functionalized or coated with different materials depending on their application. Ugelstad beads have applications in diverse areas of science and technology, *e.g.* in conductive adhesives in the electronic industry (Kristiansen *et al.*, 2004, 2005), for separating bio-reactive molecules (Ugelstad *et al.*, 1993), for fluorescence tracking inside cells (Rembaum *et al.*, 1982) and in cancer therapy (Anderson *et al.*, 1989). Both metal-coated and bare Ugelstad spheres were studied in the present work. A typical polymer used for these beads is poly(methyl-methacrylate) (PMMA). PMMA is known to be susceptible to radiation damage: fragmenting the polymer backbone creates by-products such as H^+, CH_2^+, CH_3^+ and CHO^+ (Tinone *et al.*, 1994) and the polymer experiences mass loss (Beetz & Jacobsen, 2003; Coffey *et al.*, 2002). It is also known that one of the primary radiation damage mechanisms is the breaking of C═O bonds, as this degradation is independent of the sample temperature (Beetz & Jacobsen, 2003). The oxygen mass loss is, however, correlated to the temperature, and the mass loss can be strongly reduced by decreasing the temperature (Beetz & Jacobsen, 2003). The results and methods presented here can be generalized to estimate the radiation sensitivity for future CXDI experiments where soft organic, including biological, materials are imaged. By using the experimental synchrotron techniques of 3D CXDI and XPCS, the degradation process of the polymer core could be followed at about 30 nm resolution, sufficient to directly observe the mass loss.

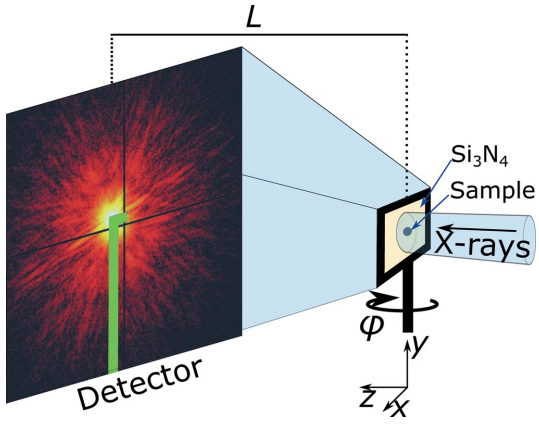

Figure 1
Sketch of the experimental setup. The micro-composite sample to be studied was electrostatically sticking to a silicon nitride membrane and illuminated by coherent X-rays. The membrane was placed on a stage which could be rotated about the *y*-axis. The scattering patterns were collected by a Maxipix detector. The L-shaped beam stop is indicated in green.

2. Experimental setup

2.1. Sample systems

The sample systems studied were (i) composite metal-coated Ugelstad polymer microspheres and (ii) bare (uncoated) Ugelstad polystyrene (PS) microspheres. Both were prepared by the Ugelstad technique (Ugelstad *et al.*, 1980). The composite microspheres consisted of a PMMA polymer core of 3 µm diameter and three layers of coating. The supplier (Conpart AS, Skjetten, Norway) specified the thicknesses of the coatings to be made of 100 nm nickel, 20 nm gold and 35 nm SiO_2, with nickel being the innermost coating, and SiO_2 the outermost. The uncoated PS sphere had a diameter of 1.19 µm. The spheres were electrostatically sticking to a 100 nm-thick Si_3N_4 membrane, purchased from Silson Ltd, and placed on a rotation stage as indicated in Fig. 1.

2.2. Coherent X-ray microscopy

The experiment was performed at the ID10 beamline at the ESRF in France. The X-ray beam energy was selected by a Si(111) monochromator after collimation by two sets of high-power slits and focused by compound refractive lenses (CRLs) (Lengeler *et al.*, 2005), located at 53.5 m from the undulator source. The sample was positioned 7.5 m downstream from the CRLs. The longitudinal coherence length was ∼0.5 µm and the transverse coherence length was ∼5 (25) µm in the horizontal (vertical) plane. The coherent part of the beam was selected by roller-blade slits (Bolloc'h *et al.*, 2002) with a 10 µm × 10 µm opening 55 cm upstream from the sample. A flight tube was positioned between the sample and detector, to reduce air scattering and absorption. The scattering patterns were collected by a Maxipix detector with 55 µm × 55 µm pixel size (Ponchut *et al.*, 2011). The intense direct beam was blocked by a beam stop to prevent damage to the detector. For the experiments with composite microspheres the photon energy was 8.10 keV (λ = 0.153 nm), the sample detector distance L = 3.235 m, and the photon rate of the beam was 5.6×10^{10} s^{-1}. For the experiments on bare PS spheres the photon energy was 7.00 keV (λ = 0.177 nm), L = 2.615 m and the photon rate 2.0×10^{10} s^{-1}.

To directly monitor the evolution of radiation damage in 3D, 14 consecutive 3D tomograms were collected of a composite microsphere. Each scan consisted of rotating the sample about the *y*-axis from −81.0° to 62.9° with respect to the incoming beam, in 0.33° steps. At each projection angle, a scattering pattern was recorded using an exposure time of 0.9 s. In addition, the microsphere was realigned in the beam every ten projections, so the total exposure time of the sample to the X-ray beam was roughly 480 s per tomogram.

The reconstruction algorithm used in this work is the Hybrid Input–Output (HIO) plus Error Reduction (Fienup, 1982), and the Shrink-Wrap algorithm (Marchesini *et al.*, 2003) for support refinement. The numerical CXDI reconstruction applies constraints in both real and reciprocal space. The first constraint is that the scattering pattern of the reconstructed object should match the measured scattering pattern, and the second is that the sample is limited by a support that represents the area/volume of the sample in the field of view. As discussed by Thibault *et al.* (2006), the reconstructed image can be decomposed into a sum of functions (or modes), because of the linearity of the Fourier transform. If a mode is constrained in space to be within the sample support, and the Fourier transform of this mode only has non-zero amplitude values where the scattering pattern is not measured, then this function is called an 'unconstrained mode'. Unconstrained modes might appear superposed on the constrained modes forming the imaged object, and can cause unrealistic density variations in the reconstructions. Non-measured scattering angles can be caused by gaps between detector modules, or by a beam stop blocking the lowest scattering angles. The upper bound to the number of unconstrained modes M can be calculated as (Thibault *et al.*, 2006)

$$M = \frac{N_S N_C}{N^3}, \qquad (1)$$

where N_S is the number of voxels inside the support, N_C is the number of unmeasured frequencies and N^3 is the number of voxels in the reconstructed cubic field of view.

The reconstructed tomograms showed artifacts caused by unconstrained modes as described above. The unconstrained modes manifested themselves as unrealistically high-density values in the core of the sphere. The reconstruction was expanded in Hermite polynomials as carried out by Thibault *et al.* (2006), but in our case only the eight strongest unconstrained modes were subtracted from the reconstruction to reduce the strongest artifacts, despite the high number of unconstrained modes in our reconstruction (>1000), as calculated from (1).

For the bare PS sphere, 165 scattering patterns were recorded, each with an exposure time of 20 s, resulting in a total accumulated exposure time of 3300 s. The size of the sphere could be measured by fitting the form factor of a perfect sphere to the experimental scattering pattern. The

measured 3D electron density distribution in the spherical composites allowed the absorbed radiation doses to be precisely estimated.

2.3. XPCS

For the XPCS analysis a series of 10000 scattering patterns from a metal-coated polymer sphere was recorded with an exposure time of 2.0 s per frame, so that the total exposure time was 20000 s. The scattering patterns were analyzed using in-house XPCS software to calculate the correlation function g_2 as described later.

3. Results and discussion

3.1. Experimental coherent scattering patterns

A representative scattering pattern of a metal-coated PMMA sphere obtained with 2.0 s exposure time is given in Fig. 2(*a*). The concentric intensity circles around the scattering pattern center are consistent with the imaged metal-coated bead having a spherical shape. The discontinuous speckled pattern at high q arises because of imperfections in the sphere. A clear beating is seen in the scattered intensity, caused by the thin metallic coating, which is also seen in the azimuthally integrated intensity (*cf.* Fig. 2*b*).

For estimating the absorbed dose, a model of the multilayer sphere was constructed with the radially varying electron density $\rho_e(r)$ fitted to the experimental scattering pattern. For optically thin objects the paraxial transmission function of an object can be calculated in the projection approximation (Dierolf *et al.*, 2010) [see also (Skjønsfjell *et al.* (2018) for a discussion],

$$T(x, y) = \exp\left\{\frac{2\pi i}{\lambda}\int \left[\delta(\mathbf{r}) + i\beta(\mathbf{r})\right] \mathrm{d}z\right\}. \quad (2)$$

Here, λ is the wavelength of the X-ray beam, δ and β are the decrements of the refractive index $n = 1 - \delta + i\beta$, and the X-rays are considered to propagate in the z-direction. δ is given by $\delta = 2\pi r_e \rho_e / k^2$ (Als-Nielsen & McMorrow, 2011), where $r_e = 2.82 \times 10^{-15}$ m is the Thomson scattering length, and $k = 2\pi/\lambda$. The wavefront ψ just after the object is then given as the product between the incoming wavefront ψ_0, often taken to be a plane wave, and the transmission function, $\psi = \psi_0 T$. In the Fraunhofer regime, the recorded scattered intensity pattern I at the detector a distance L from the sample can then be calculated as the absolute square of the Fourier transform of ψ. Note that if the phase shift experienced by the X-ray beam upon traversing the sample is small, and the kinematical approximation can be used, then the scattered intensity is given by the absolute square of the Fourier transform of the electron density distribution.

The fitted electron density and azimuthally integrated intensity of the experimental and theoretical scattering pattern can be seen in Fig. 2(*b*).

3.2. 3D CXDI of mass loss

The series of 3D tomograms revealed directly how a metal-coated sample was affected by beam damage at a resolution of ~30 nm. The exact same sample was imaged repeatedly, and only the accumulated exposure time of the bead to the X-ray beam differed between the tomograms. Fig. 3 shows cross sections at the same plane through the imaged particle, for six selected 3D tomograms. The zebra-like intensity variations are known to arise from missing low-q data, caused primarily by the missing wedge and the beam stop (Thibault *et al.*, 2006). More interestingly, one can see that a bubble of reduced density develops in the polymeric core of the composite. Because the only parameter that changed between the tomograms was the integrated exposure time, it is clear that the low-density region was caused by radiation damage. The bubble grew monotonically larger for each subsequent tomographic measurement. Fig. 4 shows a 3D rendering of the bubble inside the bead developing as a function of exposure time. Because of the faint density differences between the polymer and the bubble, the segmentation was performed manually. Despite the inherent ambiguity in the exact interpretation of each individual tomogram, the mutually consistent 3D reconstructions establish the presence of a growing low-density bubble. After an integrated exposure time of 6720 s one can see that the bubble of low-

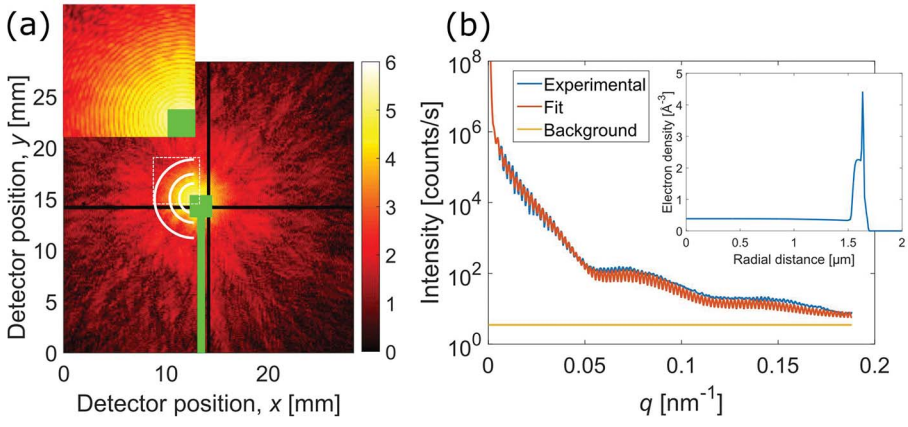

Figure 2
(*a*) A typical experimental scattering pattern from a metal-coated microsphere. The sample is close to a perfect sphere as seen from the concentric circles. The speckles originate from structural imperfections, mainly in the metallic coating. The direct beam was blocked by a beam stop, indicated by the green rod. The color scale gives the $\log_{10}$ value of the photon count per pixel per second. The white half-circles represent $q = 0.018$ nm^{-1}, 0.03 nm^{-1} and 0.05 nm^{-1}. The inset gives a magnified view of the region within the square, highlighting the concentric scattering rings. (*b*) Azimuthally integrated intensity of the experimental scattering pattern, and the calculated scattering pattern from the model sphere. The radial electron density of the model sphere is shown in the inset. The intensity beating, with period $q \simeq 0.055$ nm^{-1}, is caused by the metallic coating. The fit is in good agreement with the experimental data. A constant background of 3.5 counts s^{-1} has been added to the fitted curve.

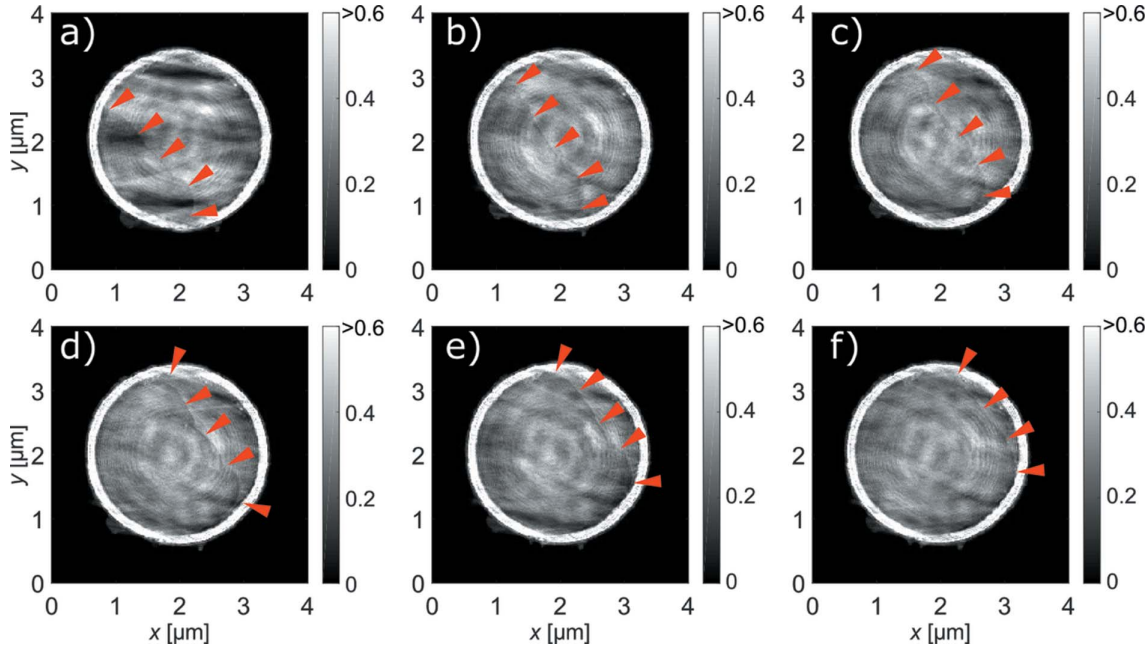

Figure 3
Tomographically reconstructed slice of the sphere in the *xy*-plane after cumulative exposure times of (*a*) 960 s, (*b*) 1920 s, (*c*) 3360 s, (*d*) 4320 s, (*e*) 5760 s and (*f*) 6720 s. (Corresponding doses: 4.2, 8.6, 15, 19, 26, 30 GGy.) A region of low-density polymer is developing in time, starting from the lower left region of these projections, as highlighted by the red arrows. The color bar gives the electron number density per cubic Ångström.

density polymer fills almost the entire core of the sphere, as indicated in Fig. 4(*e*).

Already in the first tomographic reconstruction, as seen in Fig. 4(*a*), the micro-composite had a sizable internal bubble. This initial bubble might be caused by the radiation dose delivered when aligning the sphere in the X-ray beam, and when pre-imaging the particle with scanning electron microscopy (results not shown). From the 3D images, it is evident that the bubble was developing from a hole in the coating marked with the blue arrow in Fig. 4(*f*). The fact that the bubble had a comparably large size already in the first tomogram testifies that performing high-resolution imaging on these particles is challenging because of the radiation damage.

The polymer–bubble boundary moved several pixels, corresponding to about 50 nm, between each reconstructed tomogram. Note that the reconstructed images necessarily represent an averaged structure during the time span of the tomographic measurements; it is fascinating that the CXDI reconstruction algorithm is able to provide sharp 3D images of an object that principally changes between each X-ray exposure. Consequently, it is also important to compare single exposures, during which the structure changes negligibly.

Azimuthally averaged scattering patterns for a fixed projection angle of $\varphi = 0^\circ$ from the series of tomography measurements were fitted in the same way as the scattering pattern in Fig. 2(*b*). For the last tomographic exposure, models where the density of the polymer core was 65–75% of the original polymer density gave good fits to the experimental

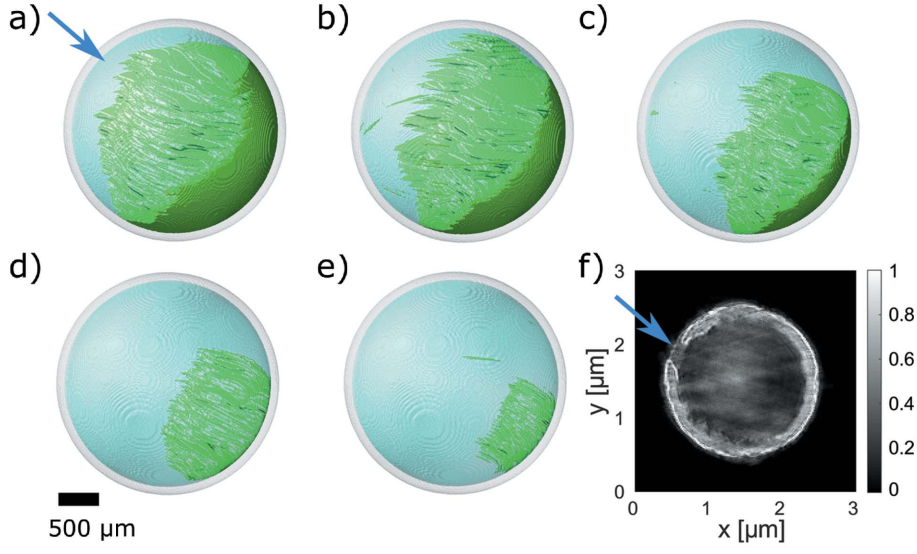

Figure 4
A series of 3D semi-transparent renderings of the polymer core. The same microsphere was exposed to the X-ray beam for (*a*) 480 s, (*b*) 1440 s, (*c*) 2880 s, (*d*) 4800 s and (*e*) 6720 s. (Corresponding doses: 2.2, 6.5, 13, 22, 30 GGy.) The painted semi-transparent silver color illustrates the metal coating, the green color represents the polymer core and the aqua color represents polymer of reduced density. After almost two hours of integrated exposure, the bubble fills 97% of the volume inside the metal coating, as seen in (*e*). (*f*) An *xy*-cross section of the first tomogram (t = 480 s) showing a hole in the coating, indicated by the blue arrow. The hole in the coating appears to be the initiation point of the bubble. The color bar gives the electron number density per cubic Ångström.

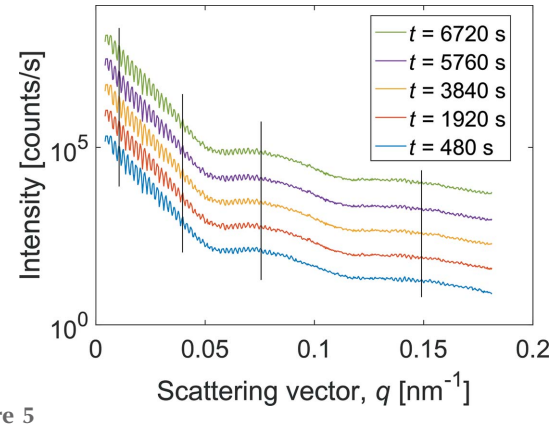

Figure 5
Azimuthally averaged scattering patterns from different tomogram series. The integrated scattering patterns are taken for the same sample projection angle $\varphi = 0°$. There are only small differences between the scattering curves. The black vertical lines have been added to help see that the local scattering maxima are at the same position for all scattering curves. Each scattering curve has been offset by a factor of five. The corresponding doses are 2.2, 8.6, 17, 26 and 30 GGy.

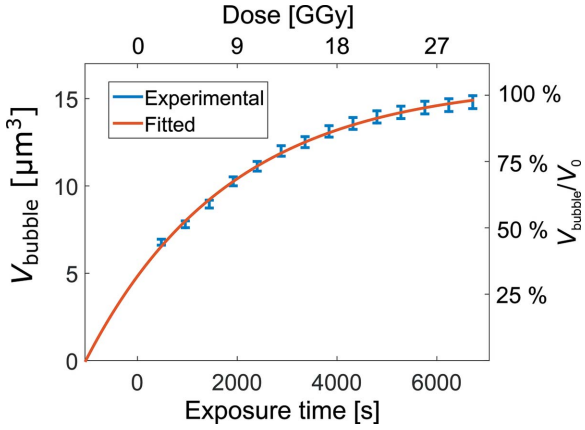

Figure 6
The volume of the low-density polymer-bubble inside the microsphere grew monotonically as a function of exposure time. After an exposure time of 6000 s the bubble filled essentially the entire volume inside the metal coating. The extrapolation to $V_{\rm bubble} = 0$ at negative times gives an estimate of the radiation dose incurred by the preliminary scanning electron microscopy and X-ray alignment steps.

scattering pattern (not shown). However, the changes between the averaged scattering patterns from the different tomography series were not large enough to draw clear-cut conclusions, as demonstrated in Fig. 5. The scattering curves are all similar, suggesting that conventional SAXS analysis is not capable of resolving the density transformation in the polymer core. Our understanding is that in the conventional SAXS approach the slight changes cannot be discerned in the azimuthally averaged (1D) single projections owing to insufficient signal-to-noise ratio. On the other hand, CXDI involves both phase retrieval, more than 430 projections and no azimuthal averaging, allowing the object to be reconstructed in 3D. The subtle density changes, notably the bubble formation, can be discerned precisely because the CXDI analysis allows the electron density to be visualized in 3D.

The volume of the bubble inside the microsphere as a function of exposure time is plotted in Fig. 6. One can clearly see that the bubble inside the microsphere is increasing as a function of time, consistent with radiation-induced mass loss. The fitted line in Fig. 6 is given by

$$V_{\rm bubble} = V_0\Big\{1 - \exp\big[-(t - t_0)/\tau_0\big]\Big\}, \qquad (3)$$

where t_0, τ_0 and V_0 are fitted to be −680 s, 2350 s and 16 μm^3, respectively, and t is the cumulated exposure time. The time constant τ_0 corresponds to a dose of 11 GGy. Describing the bubble volume in this form is motivated by the fact that it exhibits a smooth development towards the total polymer volume V_0. V_0 matches well with the measured volume of the initial polymer core of 15.5 μm^3, and t_0 gives an estimate of the effective exposure time prior to the start of the experiment.

There is a clear correlation between the development of the bubble and the outer boundary of the high-density polymer. The transformation from high- to low-density polymer starts at a hole in the metallic coating, where the polymer is exposed to air. During the X-ray exposure the boundary between the high-density polymer and low-density polymer moves, suggesting that the mass loss occurs where the high-density polymer is exposed to the low-density polymer.

3.3. Mass loss from an uncoated PS sphere

How the bare (uncoated) PS sphere lost mass and literally shrank as a result of the radiation exposure can be seen in Fig. 7. The radius of the particle decreased as the accumulated dose increased, and the development was linear. Note that this is consistent with the results presented above for PMMA: the radiation-induced mass loss takes place at the free surface. For the bare polymer particle, this implies a regular decrease of the radius with time.

As a consistency check, we note that as mass is lost from the PS sample the scattered intensity should decrease. For the data in Fig. 7, the radius decreased from 0.57 to 0.47 μm over the course of the experiment (3300 s). This corresponds to the volume decreasing to 56% of its initial value. As the SAXS intensity is proportional to the square of the particle volume, the scattered intensity should drop to $I/I_0 \simeq 31\%$. As seen in Fig. 7(*d*), the integrated scattered intensity in the forward direction ($q \simeq 0$) falls off by 44%, consistent with the fact that the radius of the sphere decreases and there being less material to scatter.

3.4. XPCS analysis

Radiation dose is proportional to the number of absorbed photons and hence to the exposure time. During the XPCS measurements the sample was continuously illuminated by X-rays. Following the almost linear decrease of the scattered intensity with exposure time (Figs. 7*c* and 7*d*), it is clear that the radiation damage is a continuous process which suggests a connection between the exposure time and the intensity correlations to be established. In other words, we assume that as a first-order approximation the response to an additional radiation dose is the same independently of the accumulated

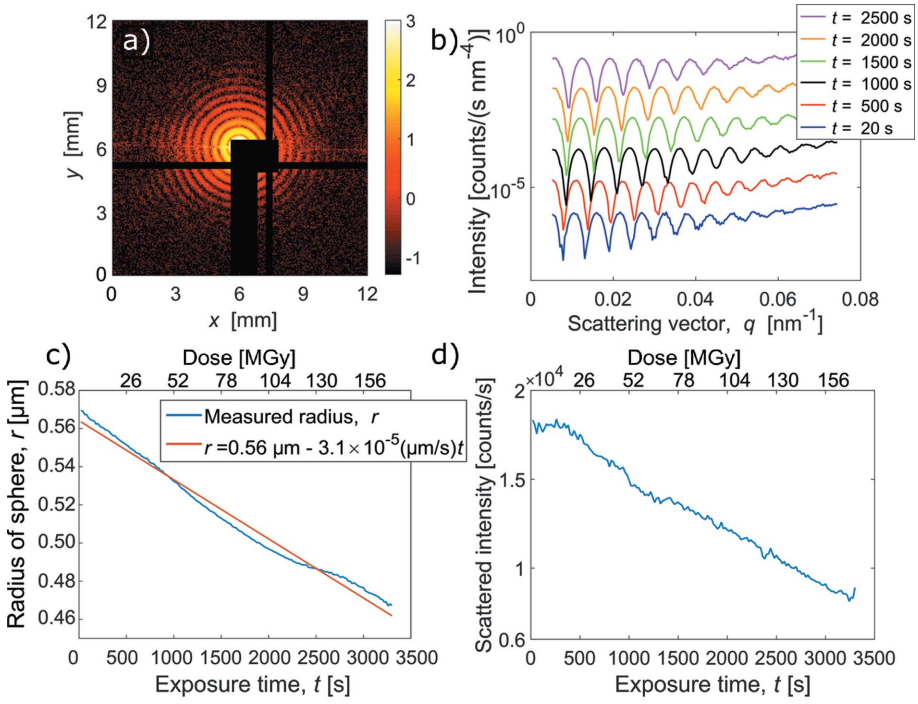

Figure 7
Scattering results for an uncoated PS sphere. (*a*) A representative scattering pattern. The color bar indicates the $\log_{10}$ photon count per pixel accumulated over 20 s. (*b*) A selection of azimuthally integrated scattering patterns, multiplied by q^4 to emphasize the Porod character of the scattering. One can see that the spatial period of the intensity oscillations increases with the accumulated exposure times, meaning that the sphere radius decreases. Each curve has been offset by a factor of ten for visibility. (*c*) Radius of the PS sphere as a function of accumulated exposure time. The decrease of the radius is well described as a linear function of time. (*d*) Scattered intensity in the forward direction. The scattered intensity was found by fitting the form factor of a perfect sphere to the experimental data. One can see that the scattered intensity falls for increasing absorbed dose, consistent with having less material scattering.

dose. These considerations motivated a separate set of XPCS measurements using the same experimental setup as for the CXDI, to study in more detail the temporal intensity correlations.

Based on long experimental time series (hours) of repeatedly capturing 2.0 s exposure diffraction patterns for a metal-coated PMMA sphere, the normalized correlation function $g_2(q,\tau)/g_2(q,0)$ was obtained using XPCS analysis. The intensity auto-correlation function g_2 calculated from the two-dimensional scattering patterns is defined by

$$g_2(q,\tau) = \frac{\left\langle \left\langle I_q(t)\, I_q(t+\tau) \right\rangle_q \right\rangle_t}{\left\langle I_q(t) \right\rangle^2_{q,t}}, \qquad (4)$$

where $I_q(t)$ is the intensity at scattering vector q at time t. τ is the lag time, $\langle \ldots \rangle_q$ and $\langle \ldots \rangle_t$ denote averaging over scattering vector and time, respectively. The measured temporal correlation functions are shown in Fig. 8(*a*). Most importantly, it is seen that there is full correlation at all q for correlation times $\tau < 100$ s, and $g_2 > 0.9$ for $\tau < 10^3$ s. This suggests a limit to the exposure time that can be used for tomographic reconstruction, consistent with the fact that an exposure time per tomogram of 480 s as used in this work provided good tomograms. It is intuitively reasonable that the intensity correlations at the highest q values, corresponding to the finest structural details, should drop first, which is indeed seen to be the case (*cf.* Fig. 8). The non-monotonic intensity $I(q)$ caused by the shell (*cf.* Fig. 2) adds complications, which is likely the reason for the oscillations seen in the correlation value g_2. We observed that the correlation had a minimum at the intermediate $q \simeq 0.050\ \mathrm{nm}^{-1}$. This is shown in Fig. 8(*a*), and is also shown with the four displayed q in Fig. 8(*b*). This minimum at $q \simeq 0.050\ \mathrm{nm}^{-1}$ corresponds to the first minimum of the envelope function of the scattering pattern, as is seen in Fig. 2(*b*). It is likely that the scattering pattern at this minimum is more sensitive to changes in the polymer density, therefore causing a decay of $g_2(q,\tau)$ at shorter delay times.

To test the hypothesis that the minimum of the correlation function at $q \simeq 0.050\ \mathrm{nm}^{-1}$ is caused by changes in the polymer, we numerically simulated a series of scattering patterns from an idealized metal-coated polymer sphere where the density of the polymer decreased with time. The initial electron density of the sphere is shown in Fig. 2(*b*). A model of the sphere motivated by the 3D CXDI measurements was constructed and the simulated density of the polymer in the core was forced to decrease in a similar way as the low-density polymer region was observed to develop in the 3D tomograms. The low-density region in the polymer was assumed to develop from a hole in the coating, as shown in Fig. 8(*c*). 5000 scattering patterns were calculated with each scattering pattern having an exposure time of 2.0 s. The total exposure time to the bead was thus 10000 s. To mimic the mass loss, the density of the polymer within a radius

$$r(t_{\mathrm{sim}}) = r_0\left[1 - \exp(-t_{\mathrm{sim}}/t_{\mathrm{d}})\right]^{1/3}, \qquad (5)$$

centered at the hole in the coating, was set equal to 75% of the original polymer density. Here, t_{sim} is the exposure time, $r_0 = 3.3$ μm and the time constant $t_{\mathrm{d}} = 7800$ s.

The XPCS results from the dataset simulating the scattering patterns from a sphere where the polymer is gradually removed are shown in Fig. 8(*d*). One can see that the model qualitatively reproduces the observed trends, in particular the minimum in correlation time at the intermediate $q \simeq 0.050\ \mathrm{nm}^{-1}$, supporting the hypothesis that the main features of $g_2(q,\tau)$ are indeed caused by the decreasing polymer density in the core of the composite. It is emphasized that only changes in the polymer density were simulated in the model. No statistical noise in the number of photon counts, changes in the metal and SiO_2 coatings or instabilities in the X-ray beam

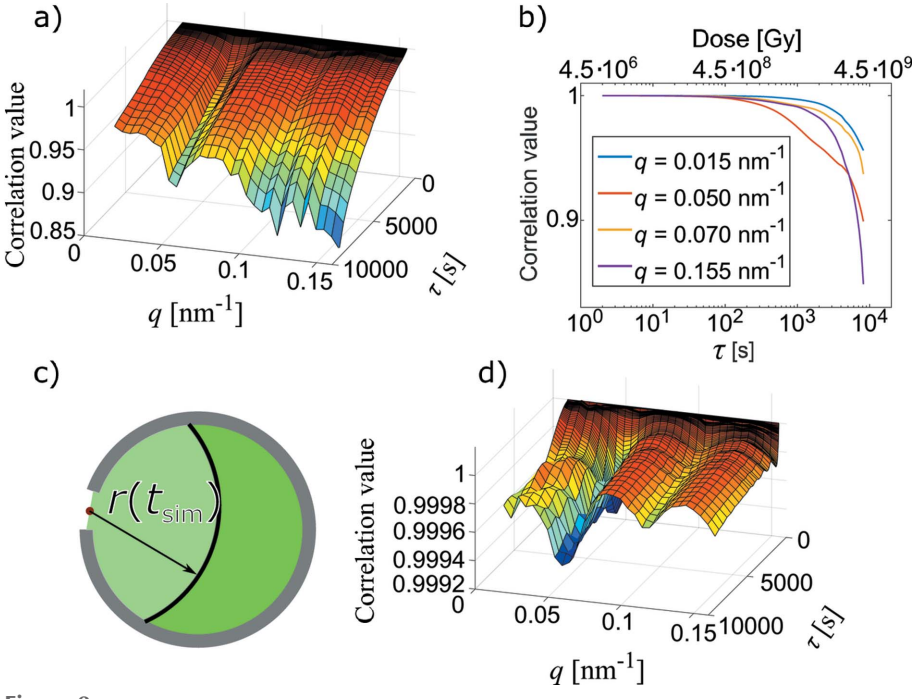

Figure 8
(*a*) 3D surface plot of the correlation value as a function of scattering vector q and correlation time τ. (*b*) Correlation curves for selected q, showing that the correlation drops significantly after $\sim$100 s (450 MGy). (*c*) Mass-loss model for the XPCS simulations. The polymer is drawn in green, while the metal coating is gray. The polymer within the volume delineated by $r(t_{sim})$ was set equal to 75% of the original polymer density, where t_{sim} represents the accumulated exposure time. The scattering pattern from the model was calculated at each time step for use in XPCS analysis. (*d*) Correlation function from the simulated dataset. The scattering pattern from a sphere where the polymer density was gradually decreased was calculated, and the XPCS functions were extracted. The correlation functions have a minimum at $q \simeq 0.05$ nm^{-1}, as in the observed XPCS curved from the experimental data.

were accounted for, all factors that would have contributed to reducing the correlations from the unrealistically high values towards the experimentally measured correlation values.

Note that the exact polymer density development in the composite measured by XPCS is unknown. No 3D CXDI measurement of the sphere was obtained, and one thus cannot know if the sphere used in the XPCS measurement degraded in a similar way as the sphere that was imaged multiple times in 3D by CXDI. Differences between the experimental and simulated dataset can be due to the fact that the sphere used in the XPCS experiment degraded somewhat differently from the sphere used in the 3D measurements. However, CXDI measurements of both coated and uncoated polymer spheres, previous observations (Bø Fløystad *et al.*, 2015) and the qualitative agreement between the CXDI and XPCS suggest a similar degradation mechanism for all spheres, where any free polymer surface acts as a site for mass loss.

For ordinary time-independent computed tomography reconstructions, the object under study cannot change significantly during the data acquisition, to prevent the reconstructions from becoming ambiguous. Assuming continuous irradiation, this effectively sets an upper limit to how long each computed tomography measurement can last. As this study demonstrates, CXDI allows discerning faint features that are not readily available from the raw data or conventional SAXS analysis. On the other hand, CXDI requires skilful data analysis and time-consuming data reconstruction. XPCS analysis as expressed in equation (4), however, gives in a straightforward manner an estimate for the structural changes for a given q during a time window τ. The elegance of using XPCS as an analytical tool for monitoring beam damage or other gradual structural changes in conjunction with CXDI experiments should thus be clear.

3.5. Final discussion

It is known that PMMA and PS are susceptible to beam damage, and, when breaking molecular bonds in the polymer, by-products such as H^+, CH_2^+, CH_3^+ and CHO^+ are produced (Tinone *et al.*, 1994). Of course, the scattering experiment presented here does not have the resolution to monitor molecular processes, but the mass loss implied by the transformation from high- to low-density polymer is readily observed. The exact molecular-scale nature of the polymer transformation from the high- to low-density state is not clear.

It can be theorized that the absorbed photon energy causes the temperature of the entire microcomposite to rise, causing the polymer to melt. The melting temperature T_m of PMMA is 378–433 K (Wypych, 2012), and it seems unlikely that the particle would reach such high temperatures by being exposed to the monochromatic X-ray beam, in particular when considering the fact that the total dose is delivered over a timespan of many hours. Yet, it has been demonstrated that the melting temperature of PMMA depends on the radiation damage, where higher doses give lower melting temperature (El-Kholi *et al.*, 2000). It is possible that the absorbed dose causes the long polymer chains to break, which lowers T_m and makes it possible for the polymer to melt (Ponomarenko *et al.*, 2011). The fact that the bubble of low-density polymer progressed from a hole in the coating might then be explained by the exposure of the polymer to a free surface (air) relaxing the constraints of motion, and thus a region of high mobility is created in the polymer close to the air–polymer interface (Keddie *et al.*, 1994). Surface melting of polymers close to the polymer–air boundary because of the increased mobility and reduced melting temperature caused by irradiation is well known (Crist, 2003). When the exposed polymer has melted, the mobility constraint decreases at the polymer melt–solid polymer interface, causing more of the solid polymer to melt. The polymer melt will thus grow as a bubble in the core of the particle, as observed by the CXDI

measurement. A detailed study of the heating process of the imaged particle by the X-ray beam has not been performed in this study. It has been noted by others that heat-transfer models are complicated when dealing with micro- or nano-sized objects irradiated by synchrotron radiation (Ponomarenko *et al.*, 2011; Vladimirsky *et al.*, 1989).

As an alternative mechanistic model for the radiation damage, one can consider electrically charged polymer fragments, literally chopped off by the X-ray beam, to fly away from the sample. Clearly, also from this viewpoint, the presence of a free surface is necessary for the reaction to proceed. Note that these models are not mutually exclusive.

Further work should be put into understanding the nature of the low-density region of the polymer core. As discussed, the density is found to be too high for the composite core to be fully void. Our best guess is that the ionizing X-ray beam changes the low-density structural stable network of the highly cross-linked polymer to be sufficiently porous to allow short polymer fragments to escape. A possibility for detailed studies could be to use either Raman scattering or near-edge X-ray absorption fine structure (NEXAFS) simultaneously with 3D CXDI. From Raman and NEXAFS one can obtain quantitative information regarding different molecular bonds and configurations. If one can correlate the development of the new molecular bonds with the low-density polymer from the 3D images, one might be able to gain further insight into the low-density polymer. This would, however, require a dedicated setup. The polymer spheres would in addition need to be smaller and without a metal coating to allow sufficient transmission of the X-ray beam at the energy levels corresponding to the covalent atomic bonds in PMMA (250–700 eV).

4. Conclusion

We have demonstrated using 3D CXDI how a metal-coated polymeric microsphere is degraded by mass loss when exposed to an intense X-ray beam for an extended period of time. It was seen from the 3D image analysis that polymer degradation with mass loss from inside the composite is the dominant radiation damage mechanism at the spatial resolution of our experiment. A low-density polymer region developed in the composite core as the radiation dose was increased. It was clear from the tomograms that the low-density polymer started to develop near a hole in the metallic coating of the particle. Consequently, minimizing the exposed polymer surface by an intact shell would presumably lead to reduced secondary radiation effects.

We have also demonstrated that XPCS can be a valuable tool for tracking structural changes in solid materials. XPCS is also particularly convenient for establishing 'safe' maximum exposure times for a given category of sample to maintain full correlation at a given q. The XPCS correlation curves $g_2(q,\tau)$ are qualitatively in full agreement with CXDI: the main features could be traced back to the polymer mass-loss in the core of the particle. Establishing a full quantitative understanding of the XPCS data would require the additional consideration of the stochastic aspects of the scattering process, notably temporal and spatial fluctuations in the sample density and in the incoming beam.

Using the same radiation dose for simultaneously imaging and damaging the micro-composite, we demonstrate that high-resolution 3D images monitoring the radiation-induced structural decay can be obtained. It is thus possible to make reliable conclusions regarding radiation damage at the tens of nanometer scale in polymeric materials as a function of dose, which is important for further development of soft-matter nanotechnology.

Acknowledgements

We are grateful to Jerome Kieffer and Pierre Paleo for help in developing fast reconstruction code for the CXDI reconstruction. David Kleiven is thanked for discussions during the experiment.

Funding information

Partial funding for this work was obtained from the Norwegian PhD Network on Nanotechnology for Microsystems, which is sponsored by the Research Council of Norway, Division for Science, under contract No. 221860/F40. The authors gratefully acknowledge the Norwegian Research Council for funding the Norwegian Resource Centre of X-ray Scattering and Imaging (RECX).

References

Als-Nielsen, J. & McMorrow, D. (2011). *Elements of Modern X-ray Physics*. New York: John Wiley and Sons.
Anderson, I. C., Shpall, E. J., Leslie, D. S., Nustad, K., Ugelstad, J., Peters, W. P. & Bast, R. C. (1989). *Cancer Res.* **49**, 4659–4664.
Beetz, T. & Jacobsen, C. (2003). *J. Synchrotron Rad.* **10**, 280–283.
Bø Fløystad, J., Skjønsfjell, E. T. B., Guizar-Sicairos, M., Høydalsvik, K., He, J., Andreasen, J. W., Zhang, Z. & Breiby, D. W. (2015). *Adv. Eng. Mater.* **17**, 545–553.
Chapman, H. N., Barty, A., Marchesini, S., Noy, A., Hau-Riege, S. P., Cui, C., Howells, M. R., Rosen, R., He, H. & Spence, J. C. (2006). *J. Opt. Soc. Am. A*, **23**, 1179–1200.
Coffey, T., Urquhart, S. & Ade, H. (2002). *J. Electron Spectrosc. Relat. Phenom.* **122**, 65–78.
Crist, B. (2003). *Macromolecules*, **36**, 4880–4890.
Dierolf, M., Menzel, A., Thibault, P., Schneider, P., Kewish, C. M., Wepf, R., Bunk, O. & Pfeiffer, F. (2010). *Nature (London)*, **467**, 436–439.
El-Kholi, A., Mohr, J. & Nazmov, V. (2000). *Nucl. Instrum. Methods Phys. Res. A*, **448**, 497–500.
Fazel, R., Krumholz, H. M., Wang, Y., Ross, J. S., Chen, J., Ting, H. H., Shah, N. D., Nasir, K., Einstein, A. J. & Nallamothu, B. K. (2009). *New Engl. J. Med.* **361**, 849–857.
Fienup, J. R. (1982). *Appl. Opt.* **21**, 2758–2769.
Grübel, G. & Zontone, F. (2004). *J. Alloys Compd.* **362**, 3–11.
Holler, M., Diaz, A., Guizar-Sicairos, M., Karvinen, P., Färm, E., Härkönen, E., Ritala, M., Menzel, A., Raabe, J. & Bunk, O. (2014). *Sci. Rep.* **4**, 3857.
Howells, M. R., Beetz, T., Chapman, H. N., Cui, C., Holton, J., Jacobsen, C., Kirz, J., Lima, E., Marchesini, S., Miao, H., Sayre, D., Shapiro, D. A., Spence, J. C. H. & Starodub, D. (2009). *J. Electron Spectrosc. Relat. Phenom.* **170**, 4–12.
Howells, M. R., Hitchcock, A. P. & Jacobsen, C. J. (2009). *J. Electron Spectrosc. Relat. Phenom.* **170**, 1–3.

Jacobsen, C. (2016). *Proceedings of the 12th International Conference on X-ray Microscopy (XRM 2014)*, p. 020035. AIP Publishing.
Jiang, H., Song, C., Chen, C.-C., Xu, R., Raines, K. S., Fahimian, B. P., Lu, C.-H., Lee, T.-K., Nakashima, A., Urano, J., Ishikawa, T., Tamanoi, F. & Miao, J. (2010). *Proc. Natl Acad. Sci.* **107**, 11234–11239.
Keddie, J. L., Jones, R. A. L. & Cory, R. A. (1994). *Faraday Disc.* **98**, 219–230.
Kristiansen, H., Gronlund, T. & Liu, J. (2004). *Proceeding of the Sixth IEEE CPMT Conference on High Density Microsystem Design and Packaging and Component Failure Analysis (HDP'04)*, pp. 259–263. IEEE.
Kristiansen, H., Zhang, Z. & Liu, J. (2005). *Proceedings of the 2005 International Symposium on Advanced Packaging Materials: Processes, Properties and Interfaces*, pp. 209–213. IEEE.
Le Bolloc'h, D., Livet, F., Bley, F., Schulli, T., Veron, M. & Metzger, T. H. (2002). *J. Synchrotron Rad.* **9**, 258–265.
Leheny, R. L. (2012). *Curr. Opin. Colloid Interface Sci.* **17**, 3–12.
Lengeler, B., Schroer, C. G., Kuhlmann, M., Benner, B., Günzler, T. F., Kurapova, O., Zontone, F., Snigirev, A. & Snigireva, I. (2005). *J. Phys. D*, **38**, A218–A222.
Livet, F. (2007). *Acta Cryst.* A**63**, 87–107.
Marchesini, S., He, H., Chapman, H. N., Hau-Riege, S. P., Noy, A., Howells, M. R., Weierstall, U. & Spence, J. C. H. (2003). *Phys. Rev. B*, **68**, 140101.
Miao, J., Amonette, J. E., Nishino, Y., Ishikawa, T. & Hodgson, K. O. (2003). *Phys. Rev. B*, **68**, 012201.
Miao, J., Ishikawa, T., Anderson, E. H. & Hodgson, K. O. (2003). *Phys. Rev. B*, **67**, 174104.
Nishino, Y., Takahashi, Y., Imamoto, N., Ishikawa, T. & Maeshima, K. (2009). *Phys. Rev. Lett.* **102**, 018101.
Ponchut, C., Rigal, J., Clément, J., Papillon, E., Homs, A. & Petitdemange, S. (2011). *J. Instrum.* **6**, C01069.
Ponomarenko, O., Nikulin, A. Y., Moser, H. O., Yang, P. & Sakata, O. (2011). *J. Synchrotron Rad.* **18**, 580–594.
Rembaum, A., Yen, R., Kempner, D. & Ugelstad, J. (1982). *J. Immunol. Methods*, **52**, 341–351.
Rodriguez, J. A., Xu, R., Chen, C.-C., Huang, Z., Jiang, H., Chen, A. L., Raines, K. S., Pryor Jr, A., Nam, D., Wiegart, L., Song, C., Madsen, A., Chushkin, Y., Zontone, F., Bradley, P. J. & Miao, J. (2015). *IUCrJ*, **2**, 575–583.
Sayre, D. & Chapman, H. N. (1995). *Acta Cryst.* A**51**, 237–252.
Sayre, D., Chapman, H. N. & Miao, J. (1998). *Acta Cryst.* A**54**, 232–239.
Schlichting, I. (2015). *IUCrJ*, **2**, 246–255.
Shapiro, D., Thibault, P., Beetz, T., Elser, V., Howells, M., Jacobsen, C., Kirz, J., Lima, E., Miao, H., Neiman, A. M. & Sayre, D. (2005). *Proc. Natl Acad. Sci.* **102**, 15343–15346.
Shen, Q., Bazarov, I. & Thibault, P. (2004). *J. Synchrotron Rad.* **11**, 432–438.
Skjønsfjell, E. T. B., Kleiven, D., Patil, N., Chushkin, Y., Zontone, F., Gibaud, A. & Breiby, D. W. (2018). *J. Opt. Soc. Am. A*, **35**, A7.
Song, C., Jiang, H., Mancuso, A., Amirbekian, B., Peng, L., Sun, R., Shah, S. S., Zhou, Z. H., Ishikawa, T. & Miao, J. (2008). *Phys. Rev. Lett.* **101**, 158101.
Starodub, D., Rez, P., Hembree, G., Howells, M., Shapiro, D., Chapman, H. N., Fromme, P., Schmidt, K., Weierstall, U., Doak, R. B. & Spence, J. C. H. (2008). *J. Synchrotron Rad.* **15**, 62–73.
Sutton, M., Mochrie, S., Greytak, T., Nagler, S., Berman, L., Held, G. & Stephenson, G. (1991). *Nature (London)*, **352**, 608–610.
Takahashi, Y., Nishino, Y., Tsutsumi, R., Zettsu, N., Matsubara, E., Yamauchi, K. & Ishikawa, T. (2010). *Phys. Rev. B*, **82**, 214102.
Takahashi, Y., Zettsu, N., Nishino, Y., Tsutsumi, R., Matsubara, E., Ishikawa, T. & Yamauchi, K. (2010). *Nano Lett.* **10**, 1922–1926.
Thibault, P., Elser, V., Jacobsen, C., Shapiro, D. & Sayre, D. (2006). *Acta Cryst.* A**62**, 248–261.
Tinone, M. C., Sekitani, T., Tanaka, K., Maruyama, J. & Ueno, N. (1994). *Appl. Surf. Sci.* **79–80**, 89–94.
Ugelstad, J., Mórk, P., Kaggerud, K. H., Ellingsen, T. & Berge, A. (1980). *Adv. Colloid Interface Sci.* **13**, 101–140.
Ugelstad, J., Mørk, P. C., Schmid, R., Ellingsen, T. & Berge, A. (1993). *Polym. Int.* **30**, 157–168.
Vladimirsky, Y., Maldonado, J., Fair, R., Acosta, R., Vladimirsky, O., Viswanathan, R., Voelker, H., Cerrina, F., Wells, G. & Hansen, M. (1989). *J. Vac. Sci. Technol. B*, **7**, 1657–1661.
Wypych, G. (2012). *Handbook of Polymers.* Toronto: ChemTec Publishing.
Xu, R., Jiang, H., Song, C., Rodriguez, J. A., Huang, Z., Chen, C.-C., Nam, D., Park, J., Gallagher-Jones, M., Kim, S., Kim, S., Suzuki, A., Takayama, Y., Oroguchi, T., Takahashi, Y., Fan, J., Zou, Y., Hatsui, T., Inubushi, Y., Kameshima, T., Yonekura, K., Tono, K., Togashi, T., Sato, T., Yamamoto, M., Nakasako, M., Yabashi, M., Ishikawa, T. & Miao, J. (2014). *Nat. Commun.* **5**, 4061.